Applied Surface Science 571 (2022) 151261

Contents lists available at ScienceDirect

Applied Surface Science

journal homepage: www.elsevier.com/locate/apsusc

Full Length Article

Structure and transport behavior of hydrothermally grown phase pure $Cu_2ZnSn_{1-x}Ge_xS_4$ (x = 0.0, 0.3) nanoparticles

Francisco Enrique Cancino-Gordillo, Julio Villanueva Cab, Umapada Pal *

Instituto de Física, Benemérita Universidad Autónoma de Puebla, Apdo. Postal J-48, Puebla, Pue. 72570, Mexico

ARTICLE INFO

Keywords:
$Cu_2ZnSn_{1-x}Ge_xS_4$ nanoparticles
Kesterite
Band tails
Hydrothermal synthesis
Electrical properties

ABSTRACT

Phase pure Cu_2ZnSnS_4 (CZTS) and $Cu_2ZnSn_{0.7}Ge_{0.3}S_4$ (CZTGS) kesterite nanoparticles of 10–35 nm size range were fabricated through a low-temperature hydrothermal process. Morphology, structure, and structural phase of the nanoparticles were determined utilizing field-emission scanning electron microscopy (FE-SEM), X-ray diffraction (XRD) and Raman spectroscopy. Electrical transport behaviors of the pelletized nanostructures were studied in a physical properties measurement system (PPMS) in the 100–320 K temperature range. Obtained results indicate that both the CZTS and CZTGS nanostructures have p-type conductivity, with high room temperature hole concentration and carrier mobility. Substitution of 30% Sn by Ge enhances the electrical conductivity of CZTS about four times. While the room temperature hole mobility in the kesterite nanostructures reduces to about 60%, the hole concentration increases about one order on Ge incorporation. The limited substitution of Sn atoms by Ge does not affect the position of acceptor levels in the electronic band gap of the kesterite nanostructures. However, it increases the concentration of Cu_{Zn} and Zn_{Cu} antisite defects and affects the transition temperature where the electrical transport of kesterite nanostructures changes from lattice scattering controlled to defect scattering controlled conduction.

1. Introduction

The quaternary chalcogenide Cu_2ZnSnS_4 (CZTS) is an attractive material for utilization in the absorber layers of thin film solar cells, with potential for replacing conventional absorber materials such as CdTe and $CuIn_xGa_{1-x}S_2$ (CIGS). CZTS is an intrinsic p-type semiconductor containing earth-abundant elements of low toxicity with a direct optical band gap energy close to 1.5 eV and high optical absorption coefficient in the visible spectra range ($\sim 10^4$ cm^{-1}) [1–5]. Currently the certified record efficiency of quaternary chalcogenide solar cells fabricated using sulfur (CZTS) and selenium (CZTSe) are 11.1% [6] and 12.6% [7], respectively, which are still much lower than the maximum efficiency of CIGS solar cells which is above 25% [8]. Generally, CZTS kesterite contains several intrinsic defects induced by off-stoichiometric composition (i.e., Cu/(Zn + Sn) < 1.0 and Zn/Sn > 1.0), which significantly influence its electrical and optical behaviors. The defects include Cu, Zn, Sn or S vacancies (V_{Cu}, V_{Zn}, V_{Sn}, or V_s), copper and zinc interstitials (Cu_i and Zn_i), anti-sites (Cu_{Zn}, Zn_{Cu}, Zn_{Sn}, Cu_{Sn}, Sn_{Cu}, Zn_{Sn} and Sn_{Zn}), and several defect complexes, depending on the deviation in cation ratio in the material [9–11]. Typically, CZTS thin films of Cu-poor and Zn-rich (Cu/(Zn + Sn) ≈ 0.8 and Zn/Sn ≈ 1.2) stoichiometry have been utilized in solar cells as these conditions generate V_{Cu} and Zn_{Cu} that increase the carrier concentration and conductivity of the absorber layer. On the other hand, the defects such as V_{Zn}, V_{Sn}, V_s, Sn_{Cu}, Sn_{zn}, Cu_{Sn}, Zn_{Sn}, Cu_i, and Zn_i are unfavorable for solar cells, as they affect the charge recombination process negatively. Among these defects, Zn_{Cu} and Cu_i form shallow donor levels near the conduction band, while V_{Zn}, V_{Sn}, V_s, Sn_{Cu}, Sn_{zn}, Cu_{Sn}, Zn_{Sn} and Zn_i form deep-level states in the band gap, acting as trapping or recombination centers. Formation of recombination centers causes a reduction of carrier lifetime, resulting in an increase of dark current (J_0) of solar cells and hence reduces its open circuit voltage (V_{oc}). In fact, one of the limitations of kesterite CZTS in solar cell application is the large deficit in V_{oc} because of several nonideal recombination losses at deep-level states [8,12]. The principal cause of recombination loss in kesterite CZTS is the change in the oxidation state of Sn from +4 to +2 during device operation under illumination. The change in the oxidation state of Sn occurs due to the perturbation of charge balance in crystal lattice during the generation of photoinduced charge carriers. From the solar cell application point of view, the reduction of Sn^{4+} to Sn^{2+} is equivalent to the formation of an

* Corresponding author.
E-mail address: upal@ifuap.buap.mx (U. Pal).

https://doi.org/10.1016/j.apsusc.2021.151261
Received 15 April 2021; Received in revised form 23 August 2021; Accepted 9 September 2021
Available online 17 September 2021

electron trap inside the band gap. The reduction can occur in two ways; the first is when Sn^{4+} is reduced in its native crystallographic position (Sn_{Sn}) and the second is when Sn^{4+} is reduced in a defect site, such as an antisite. When Sn occupies the Zn site, a Sn_{Zn} antisite defect is formed, which can produce two types of deep levels depending on the oxidation state of Sn. When Sn has an oxidation state 4+, the Sn_{Zn} antisite defect forms a double donor (Sn_{Zn}^{2+}) state inside the band gap, which can trap photogenerated electrons, reducing Sn^{4+} ion to Sn^{2+}. On the other hand, when the Sn atom has oxidation state 2+, the Sn_{Zn} antisite defect forms an isoelectronic center (Sn_{Zn}^{0}) that can trap holes [12]. Therefore, for applying CZTS in solar cell efficiently, it must be grown under the conditions that reduce the possibility of formation of antisite defect centers and the reduction of Sn^{4+} to Sn^{2+}. In this regard, a partial substitution of Sn by an element of the same group with a unique oxidation state such as Ge, is considered as a viable solution to this problem [13–18].

Incorporation of Ge in CZTS causes the formation of $Cu_2ZnSn_{1-x}Ge_xS_4$ (CZTGS) and inhibits the formation of unfavorable defects such as V_{Sn}, Cu_{Sn}, Sn_{Cu}, Zn_{Sn}, Sn_{Zn} due to the unique oxidation state of Ge and its small radius [8,12,19,20]. The tetravalent Ge^{4+} ion cannot exchange electrons with the cations such as Zn^{2+} and Cu^{1+} as occurs in the Sn^{2+} case. Furthermore, the most stable oxidation state of Ge is 4+, so the transformation from Ge^{4+} to Ge^{2+} state hardly occurs. Hages et al. synthesized $Cu_2Zn(Sn_{1-y}Ge_y)(S_xSe_{1-x})_4$ nanocrystals replacing 0% ($Cu_2ZnSnS_{0.2}Se_{3.8}$) and 30% ($Cu_2ZnSn_{0.7}Ge_{0.3}S_{0.2}Se_{3.8}$) of Sn by Ge for utilizing in solar cells [16]. The solar cells fabricated with the former sample revealed 0.41 V open circuit voltage (V_{oc}) with 8.4% internal conversion efficiency, while the cells fabricated with the latter sample revealed 0.46 V open circuit voltage and 9.4% internal conversion efficiency. On the other hand, Giraldo et al. reported a conversion efficiency of 10.1% and 0.453 V open circuit voltage for their solar cells fabricated with sputter deposited $Cu_2ZnSn_{0.8}Ge_{0.2}Se_4$ thin film [17]. Recently, Shinho et al. reported a record ~12.3% of internal conversion efficiency with 0.527 V open circuit voltage for their solar cells fabricated using $Cu_2ZnSn_{0.78}Ge_{0.22}Se_4$ thin films [18]. In all the above-mentioned works, the authors reported an enhancement of V_{oc} due to partial substitution of Sn by Ge.

Furthermore, the direct optical band gap energy of CZTS can be tuned by replacing Sn with Ge. On substitution of Sn by Ge, the optical band gap of $Cu_2ZnSn_{1-x}Ge_xS_4$ can be tuned from 1.5 to 2.2 eV in quasi-linear way with the increase of x value [19–23]. However, high concentration of Ge in $Cu_2ZnSn_{1-x}Ge_xS_4$ ($x \geq 0.25$) can generate its nanostructures or thin films with tetragonal (kesterite) and orthorhombic mixed phase [20]. Segregation of secondary phases such as ZnS and Cu_xS can also occur for $x \geq 0.8$ [13]. Moreover, substitution of Sn by Ge in high concentration induces deep-level defects due to the formation of Sn vacancies (V_{Sn}) [15,24]. Therefore, a limited substitution Sn by Ge ($x \leq 0.5$) is recommended for fabricating $Cu_2ZnSn_{1-x}Ge_xS_4$ nanostructures and thin films in pure kesterite phase with reduced defect contents [15].

Several researchers have tried to fabricate Cu_2ZnSnS_4 [25–29] and $Cu_2ZnSn_{1-x}Ge_xS_4$ [19,20,22,30] nanostructures with special attention on the control of stoichiometry, shape, size, and structural phase, encountering difficulties in preserving the kesterite phase for higher x values. Apart from synthesizing these nanostructures with controlled structure and composition, controlling electrical transport behavior is very important for their application in photovoltaic devices. While the room temperature electrical properties of $Cu_2ZnSn_{1-x}Ge_xS_4$ thin films prepared by physical deposition methods such as sputtering and thermal evaporation have been reported in the literature [31–34], only a few works have been published on the electrical behaviors of $Cu_2ZnSn_{1-x}Ge_xS_4$ nanocrystals [20,22,35]. Moreover, the works reported on the electrical properties of $Cu_2ZnSn_{1-x}Ge_xS_4$ nanostructures and nanostructured thin films correspond to their room temperature behaviors. As the pursuance of the development $Cu_2ZnSn_{1-x}Ge_xS_4$ nanostructures is basically meant for applying them in solar cells, which often operate in a variable temperature range depending on the geographical location and season change of the locations of application, it is important to know the electrical transport behavior of these nanostructures beyond room temperature. In fact, a study on the electrical transport behavior of $Cu_2ZnSn_{1-x}Ge_xS_4$ nanostructures at different temperatures is important not only in the context of their photovoltaic applications, but also to understand how the defect structures control carrier transport in them.

Here we present the electrical transport properties of $Cu_2ZnSn_{1-x}Ge_xS_4$ (x = 0.0 & 0.3) nanoparticles in the 100–320 K temperature range. The nanoparticles were grown by a low-temperature hydrothermal process using germanium tetrachloride as a Ge precursor. The structure, crystallinity, and structural phases of the nanoparticles were analyzed by X-ray diffraction (XRD) and Raman spectroscopy. Morphology and elemental composition of nanoparticles were analyzed by scanning electron microscopy (SEM) and X-ray energy dispersive spectroscopy (EDS), respectively. Effect of Ge incorporation on the defect structure and transport behaviors of the CZTS nanocrystals are discussed. Incorporation of Ge is seen to cause an early transition from lattice scattering controlled conduction to hopping conduction due to an enhancement of Cu_{Zn} and Zn_{Cu} antisite defects concentration.

2. Experimental

2.1. Reactive & solvents

Zinc acetate dihydrate ($Zn(CH_3COO)_2{\cdot}2H_2O$, J.T. Baker, 99%), copper acetate ($Cu(CH_3COO)_2{\cdot}H_2O$, Sigma-Aldrich, ≥98%), tin chloride pentahydrate ($SnCl_4{\cdot}5H_2O$, Sigma-Aldrich, 98%), germanium tetrachloride ($GeCl_4$, Sigma-Aldrich, 99.9999%), ethylenediamine ($C_2H_8N_2$, Sigma-Aldrich, ≥98%), sublimed sulfur powder (S, Fermont, 99.95%), and acetone (C_3H_6O, J.T. Baker, ≥99.5%) were acquired from the market. Deionized water from a Millipore system ($\rho > 10^{18}$ Ohm cm) was used for the synthesis of the fabricated nanostructures. All reagents were utilized as received, without further purification.

2.2. Fabrication of nanoparticles

A low-temperature hydrothermal process was adopted for the synthesis of Cu_2ZnSnS_4 (CZTS) and $Cu_2ZnSn_{0.7}Ge_{0.3}S_4$ (CZTGS) nanoparticles, following the method reported in the literature [22]. Due to the highly reactive nature of $GeCl_4$ towards atmospheric humidity, a $GeCl_4$–acetone mixture of 1:31 M ratio was prepared in a glove box under Ar atmosphere and magnetic stirring (6 h) to utilize as germanium precursor. A typical synthesis process included the dissolution of copper acetate (4 mmol), zinc acetate (2 mmol), germanium precursor ($GeCl_4$–acetone mixture) and tin chloride pentahydrate ($GeCl_4 + SnCl_4$ = 2.2 mmol) in 10 mL of deionized water under magnetic stirring. Separately, a sulfur solution was prepared by dissolving the sublimed sulfur powder (12 mmol) in 10 mL of ethylenediamine under magnetic stirring. The two solutions were mixed and transferred to a 30 mL Teflon container. The Teflon container was capped and placed inside a stainless-steel autoclave. The sealed autoclave was placed inside a Lindberg Blue gravity furnace and heated to 200 °C (at 3 °C/min). After 24 h of heating, the reactor was cooled down to room temperature. The generated solid product was separated and washed repeatedly with acetone under centrifugation (7000 rpm, 10 min). Finally, the product was dried at 60 °C for 8 h and used for further characterizations.

2.3. Characterization

X-ray diffraction (XRD) patterns of the powder samples were recorded in a Bruker D8 Discover diffractometer using CuKα radiation (λ = 1.5406 Å). The spectra were recorded at 0.02°/step with a scan rate of 2″/step in the 2θ range 10–80°. The samples were inspected in a JEOL JSM-7800F field-emission scanning electron microscope (FE-SEM) coupled with X-Max (Oxford Instruments) spectrometer for energy dispersive spectroscopic (EDS) analysis. For the SEM-EDS analysis, the

samples were prepared by placing a drop of ethanol dispersed nanostructures over silicon substrate and drying at room temperature. After that, the silicon substrates covered with the nanoparticle samples were attached with the sample holder for SEM and EDS analysis. Morphology and crystallinity of the nanostructures were analyzed by recording their low- and high-resolution transmission electron microscopic (TEM and HR-TEM) images in a JEOL 2100F microscope operating at 200 keV. For TEM analysis, the samples were dispersed over carbon-coated copper grids by drop-casting the colloidal suspension of the nanoparticles (in ethanol). A Horiba Lab Ram HR spectrometer equipped with 633 nm He-Ne laser and a thermoelectrically cooled charge-coupled device (CCD) detector was used for recording the Raman spectra of the samples. Room temperature diffuse reflectance spectra (DRS) of the samples were recorded in a Cary-5000 spectrophotometer (Varian) with diffuse reflectance accessory (integrating sphere DRA-CA-30I) attachment. To study the electrical properties of the powder samples, solid pellets of 10 mm diameter and about 0.5 mm thick were fabricated by cold pressing the powders in a pellet press die (Specac) under 3 ton pressure for 15 min. Au contacts (~1.1 mm diameter and ~50 nm thick dots) were deposited over the pellets by r.f. sputtering of an Au target. A DynaCool-9 (Quantum Design) physical property measurement system (PPMS) was utilized to measure the electrical conductivity and Hall voltage of the samples in 100–320 K temperature range, in four-point probe configuration.

3. Results and discussion

Typical SEM images of the synthesized CZTS and CZTGS nanostructures are presented in Fig. 1a, b. Formation of nanometer size quasi-spherical particles in both samples can be perceived in the micrographs. Typical EDS spectra of the samples are presented in Fig. 1c. While the EDS spectrum of the CZTS sample revealed Cu, Zn, Sn, S and C signals, the CZTGS samples revealed Cu, Zn, Sn, Ge and S signals along with adventitious C. The emission band appeared around 1.7 KeV in both the samples corresponds to the silicon substrates used to support the samples for SEM-EDS analysis. EDS estimated elemental composition of the CZTS and CZTGS nanostructures are presented in Table 1. As can be noticed, both the samples grown with Cu-poor and Zn-rich ($Cu/(Zn + Sn + Ge) \leq 1$ and $Zn/(Sn + Ge) \geq 1$) stoichiometry, which is ideal for their application in the absorber layers of solar cells [8]. The EDS estimated $Ge/(Sn + Ge)$ ratios (Table 1) in the samples matched perfectly to the corresponding nominal mol fractions of the precursors in the reaction mixtures, which indicates that almost all the Ge atoms were incorporated into the kesterite lattice by substituting Sn atoms.

TEM and high-resolution TEM (HR-TEM) analyses were performed on the samples to monitor their crystallinity and structural phase (Fig. 2). The TEM images of CZTS and CZTGS samples also revealed the formation of dispersed, quasi-spherical nanoparticles in the samples (Fig. 2a, d). Size distribution histograms of the nanoparticles prepared using corresponding TEM micrographs revealed 9.6 ± 2.3 nm and 10.7 ± 3.4 nm average particle sizes for the CZTS and CZTGS samples, respectively. Nanoparticles of both the samples revealed their good

Table 1
EDS estimated elemental composition and cation mole fractions in the kesterite nanoparticles.

Sample	Cu (at %)	Zn (at %)	Sn (at %)	Ge (at %)	S (at %)	Cu/(Zn + Sn + Ge)	Zn/(Sn + Ge)	Ge/(Sn + Ge)
CZTS	26.06	14.10	12.31	–	47.54	0.98	1.15	0.0
CZTGS	27.39	16.34	7.72	3.85	44.71	0.98	1.41	0.33

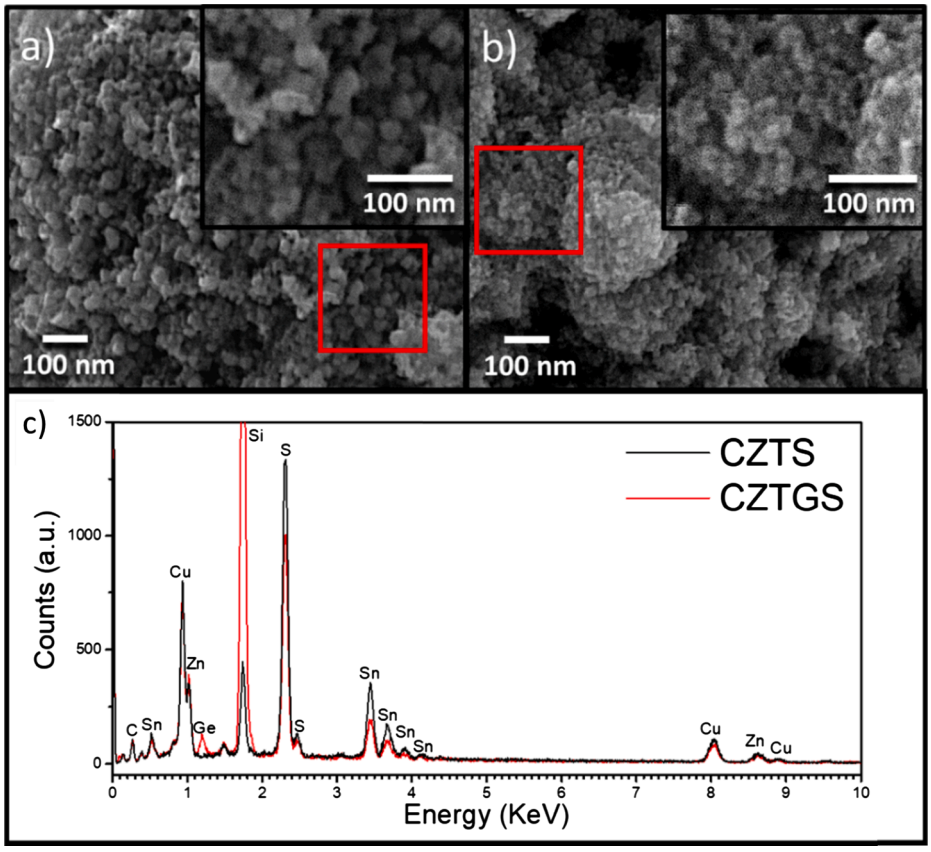

Fig. 1. Typical SEM images of (a) CZTS and (b) CZTGS nanostructures. Magnified images of selected sections (red square) are shown in the insets. Typical EDS spectra of the samples are presented in (c).

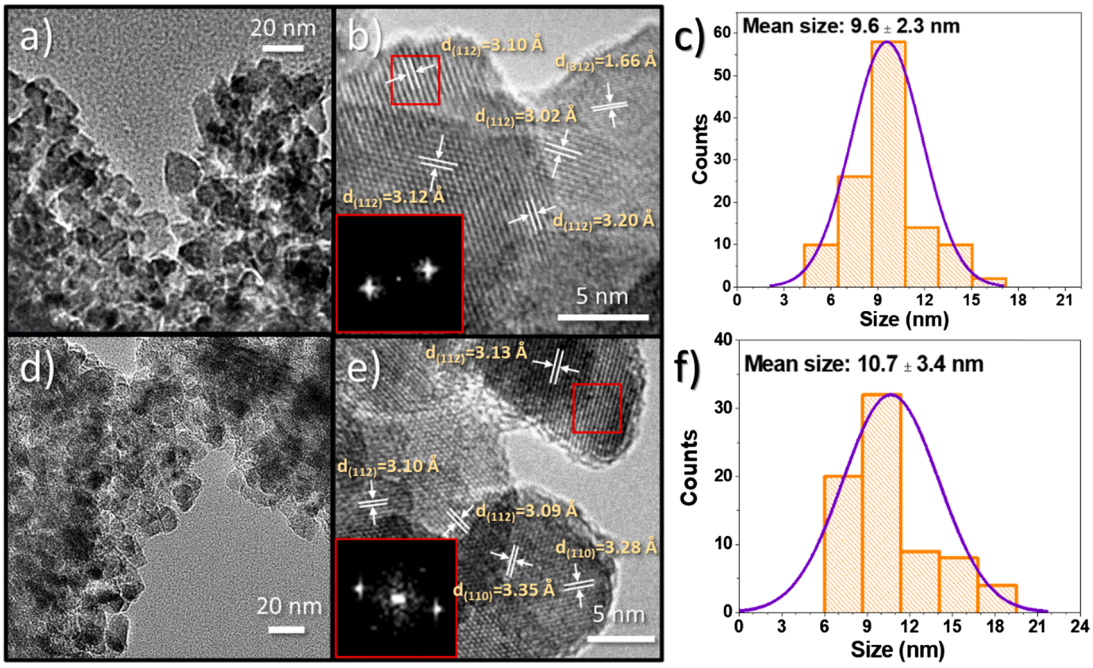

Fig. 2. Typical low- and high-resolution TEM micrographs and corresponding size distribution histograms of (a-c) CZTS and (d-f) CZTGS nanoparticles. The insets in the HR-TEM micrographs are the FFT patterns of selected areas (red square zones) of the samples.

crystallinity, with well-resolved atomic planes in their HR-TEM micrographs (Fig. 2b, e) and well-defined diffraction spots in their fast Fourier transform (FFT) patterns (inserts of Fig. 2b, e).

Room temperatures XRD patterns of the samples are presented in Fig. 3. XRD pattern of both the samples revealed well-resolved diffraction peaks around 28.74, 33.28, 47.78, 56.62, 69.21, and 76.53° Bragg angles, which correspond to the (1 1 2), (2 0 0), (2 2 0), (3 1 2), (4 0 0) and (1 3 6) lattice planes, respectively, of CZTS in tetragonal kesterite phase (PDF # 04-017-3032). Although both the CZTS and CZTGS samples revealed the same diffraction bands (i.e., the diffraction bands of the same Miller indices), their peak positions in the latter sample are slightly shifted towards higher angles in comparison to their positions in the former sample. Such a higher angle shift of the diffraction peaks for the CZTGS sample is expected as the unit cell volume of the kesterite lattice shrinks due to the substitution of Sn atoms of higher ionic radius (ionic radius of Sn^{4+} is 0.69 Å) [36] by the Ge atoms of smaller ionic radius (ionic radius of Ge^{4+} is 0.39 Å) [20–23].

Several structural parameters of the CZTS and CZTGS nanoparticles were extracted by Rietveld refinement of their XRD patterns using GSAS-II software (version 4379) [37]. The Rietveld analysis used pseudo-Voight function, the kesterite structure with space group $I\bar{4}$ (PDF # 04-017-3032), and Chebyshev polynomial-based background construction to obtain the lattice parameters and grain size. The quality of refinement and reliability of the extracted parameters were validated by measuring the goodness of fitting (GoF), which is the ratio of the weighted profile R-factor (R_{wp}) and expected R-factor (R_{exp}), where R is

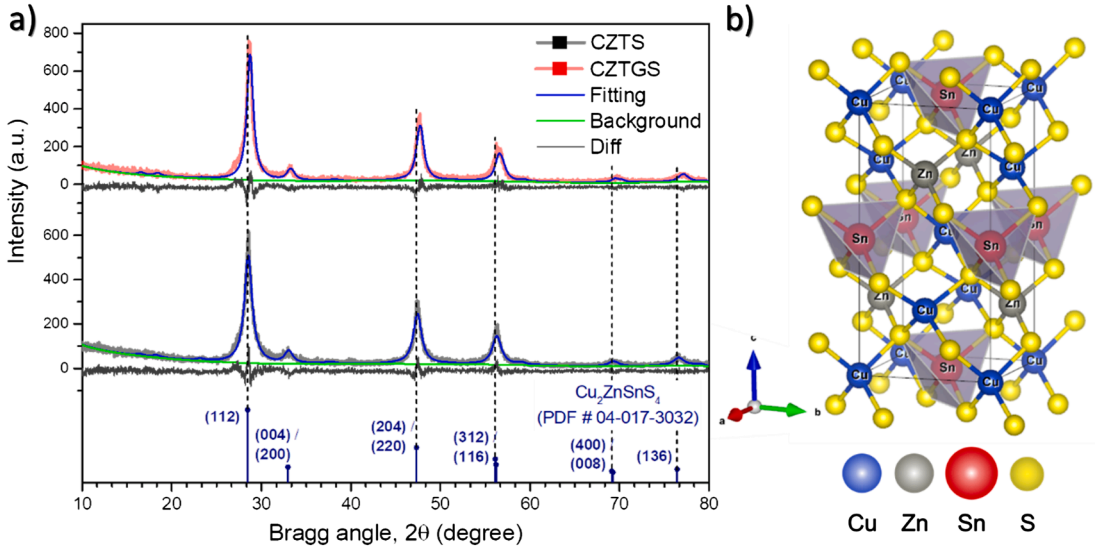

Fig. 3. (a) Rietveld analysis output profiles of CZTS and CZTGS nanoparticles fabricated by hydrothermal process and (b) schematic presentation of the kesterite lattice, highlighting the tetrahedral sites occupied by Sn cations. The blue, gray, red and yellow spheres correspond to Cu, Zn, Sn, and S atoms in the kesterite lattice, respectively.

the square root of the quantity minimized [38]. The GoF and R_{wp} values of the fitted patterns for the CZTS and CZTGS samples are 1.15 with 15.0% and 1.21 with 15.66%, respectively. As we can see, the GoF values for the samples are not exactly 1.0 (the ideal value), which probably due to high noise signal of the experimental diffraction patterns. Moreover, the materials (CZTS and CZTGS nanostructures) have a relatively complex atomic structure (Fig. 3b) for which the conventional XRD analysis cannot provide sufficient information about the positions and occupation fraction of the atoms in the kesterite structure, which we discussed latter [39]. While a high noise signal in the experimental XRD pattern introduces uncertainties in Rietveld refinement, and hence in the estimated values of lattice parameters, it also increases the GoF value [38]. The experimental and refined XRD data of the samples are plotted in Fig. 3 and the extracted structural parameters such as lattice constants, grain size, microstrain and mass density are presented in Table 2. As can be noted, the average grain size of the CZTGS nanocrystals (11.0 nm) is a bit larger than the average grain size of the CZTS nanocrystals (9.0 nm), although both the samples were synthesized under similar experimental conditions. The nucleation and growth rates of kesterite nanocrystals depend on the nature of used solvent and the precursors [40]. As the metal ions such as Zn^{2+} and Ge^{4+} form stronger bonds with Cl^- ions in comparison with the CH_3COO^- ions, utilization of metal acetate precursors induces faster nucleation and growth of the kesterite particles than when their chloride precursors are utilized. In the present case, we utilized zinc acetate and copper acetate as zinc and copper precursors, respectively. On the other hand, tin chloride and germanium chloride were utilized as tin and germanium precursor, respectively. In the present case, we utilized a mixture of $GeCl_4$ and acetone as germanium precursor. The Lewis acid $GeCl_4$ mixed with acetone forms a stable organometallic species with relatively weak Ge^{4+} - oxygen bond [41]. On the other hand, ethylenediamine was utilized in the reaction mixture (to dissolve sulfur powder). Therefore, the $GeCl_4$-acetone complex coordinates with the ethylenediamine to form a new complex with six-coordinated Ge ion [41]. This new complex possesses low thermal stability, and consequently during hydrothermal process, the Ge^{4+} ions incorporate in the kesterite lattice in faster rate, inducing a larger grain growth in the CZTGS nanostructures.

All the peaks revealed in the XRD patterns of the samples correspond to the kesterite phase, indicating their high structural purity. The quaternary CZTS and CZTGS can acquire two crystal structures, kesterite (space group $I\bar{4}$) and stannite (space group $I\bar{4}2m$), depending on the distribution of Cu and Zn cations in their lattice. However, if the Zn and Cu ions are randomly distributed in the lattice, a disordered kesterite structure can be formed with both the kesterite and stannite phases [39,42,43]. Due to the small difference in atomic scattering form factors (f) of Cu^+ and Zn^{2+} cations (the cations have the same number of electrons and f is proportional to the atomic number) it is impossible to distinguish these phases (kesterite and stannite) in their XRD patterns, which might be another reason for the high GoF values of the Rietveld fittings of the samples [39]. Also, the nonstoichiometric conditions such as Cu-poor and Zn-rich, can lead to the coexistence of disordered kesterite, along with the formation of binary or ternary sulfides such as ZnS, $Cu_{2-x}S$ or Cu_2SnS_3 in the samples [44–47]. As all these compounds posse similar crystal structures and hence produce almost identical diffraction patterns, conventional XRD analysis alone cannot ensure the phase purity of the CZTS and CZTGS nanostructures. Therefore, to investigate further the phase purity of the synthesized nanostructures along with structural disorder, we performed their Raman spectroscopy at room temperature.

Table 2
Structural parameters of CZTS and CZTGS nanoparticles extracted from Rietveld analysis of their XRD patterns.

Structural parameter	CZTS	CZTGS	Cu_2ZnSnS_4 (PDF#04-017-3032)
a (Å)	5.43	5.41	5.43220
c (Å)	10.81	10.72	10.8431
Unit cell volume (Å^3)	318.2	314.3	319.98
Grain size (nm)	9	11	–
Microstrain (10^{-6})	539.0	679.3	–
Density (g/cm^3)	4.58	4.48	4.56

Room temperature Raman spectra of the kesterite nanostructures are presented in Fig. 4a. Raman spectra of both the samples revealed an intense dispersion band around 330 cm^{-1}. However, the dispersion band is considerably wide and contains multiple humps at lower and higher energy sides. To analyze the contribution of other dispersion modes in the 330 cm^{-1} signal, the Raman bands of both samples were computer-deconvoluted using Lorentzian curve fitting analysis (Fig. 4a). We can see that the principal Raman dispersion band of the CZTS sample contains three components, peaked around 280, 330, and 357 cm^{-1}. According to the literature, the principal Raman dispersion bands of stoichiometric Cu_2ZnSnS_4 single crystals, the so-called A vibrational modes are located at 287 and 337 cm^{-1} [48–50]; and for non-stoichiometric, e.g., Cu-poor and Zn-rich Cu_2ZnSnS_4, these A modes shift towards lower wavenumbers [51]. The component bands revealed around 280 and 330 cm^{-1} we assigned to the rotation and stretching vibrations of Sn-S bonds (A modes) in the SnS_4 tetrahedron of CZTS, respectively [48–50]. The movements of anions in rotation and stretching vibration modes are presented schematically in Fig. 4b. The component band located at 357 cm^{-1} corresponds to the displacement of cations along the c axis direction, commonly known as B vibrational mode of CZTS [48–50]. On the other hand, substitution of Sn by Ge in the kesterite lattice (CZTGS) modifies the force constants of the Ge-S and Sn-S bonds because of mass and size differences of the Sn^{4+} (m = 118.7 amu, r = 0.69 Å) and Ge^{4+} (m = 72.6 amu, r = 0.39 Å) ions. Consequently, the dispersion bands are slightly shifted towards higher wavenumbers (blue-shift) [20–23,52,53]. As can be noticed in the Raman spectrum of the CZTGS nanostructures presented in Fig. 4, the component bands are shifted towards higher wavenumbers, clearly indicating the substitution of Sn by Ge in the kesterite lattice. To inspect the phase and composition homogeneity in the synthesized nanostructures, we recorded multiple Raman spectra of each sample at different zones (not presented), finding no significant change in the position and shape of the principal dispersion band (around 330 cm^{-1}). Raman spectroscopy analysis of the samples indicates that the CZTS and CZTGS nanostructures synthesized by our low-temperature hydrothermal process are of high purity, well-crystalline, and free from detectable binary or ternary sulfide (secondary phase).

According to theoretical reports [54–57], in Cu_2ZnSnS_4, the Cu_{Zn} antisite, (Cu_{Zn} + Zn_{Cu}), (2Cu_{Zn} + Sn_{Zn}) and (V_{Cu} + Zn_{Cu}) defect complexes have the low formation energy (0.2, 0.4, 0.55 and 0.6 eV, respectively). When the Cu/(Zn + Sn) and Zn/Sn ratios in the Cu_2ZnSnS_4 is close to one (i.e., Cu/(Zn + Sn) ≈ 1 and Zn/Sn ≈ 1), intrinsic defects with low formation energy such as Cu_{Zn} antisite, (Cu_{Zn} + Zn_{Cu}), and (2Cu_{Zn} + Sn_{Zn}) are formed. The concentration of these defects decreases when the stoichiometry of CZTS becomes Cu-poor, Zn-rich, and Sn-poor [54–57].

CZTS nanostructures of Cu-poor and Zn-rich stoichiometry (close to Cu/(Zn + Sn) = 0.8 and Zn/Sn = 1.2) are frequently utilized in photovoltaic devices due to the lower contents of Cu_{Zn} antisite and (2Cu_{Zn} + Sn_{Zn}) defect complex in them, which favors the formation of (V_{Cu} + Zn_{Cu}) defect complex. In the present study, the sample without germanium (i.e., Cu_2ZnSnS_4) has a Cu-poor and Zn-rich stoichiometry with Cu/(Zn + Sn) = 0.98 and Zn/Sn = 1.15. However, as the Cu deficiency in the sample only marginal (not very high), neutral (Cu_{Zn} + Zn_{Cu}) and (2Cu_{Zn} + Sn_{Zn}) defect complexes are formed and the content of (V_{Cu} + Zn_{Cu}) defect complex is low. On the other hand, although the sample with germanium ($Cu_2ZnSn_{0.7}Ge_{0.3}S_4$) is also Cu-poor and Z-rich, it has a higher Zn content (Table 1) than in the Ge-free sample (CZTS), and hence an increase in Zn_{Cu} antisite concentration is expected. Therefore, a reduction of (2Cu_{Zn} + Sn_{Zn}) concentration and an increment of (V_{Cu} + Zn_{Cu}) defect complex concentration are expected in the sample. The

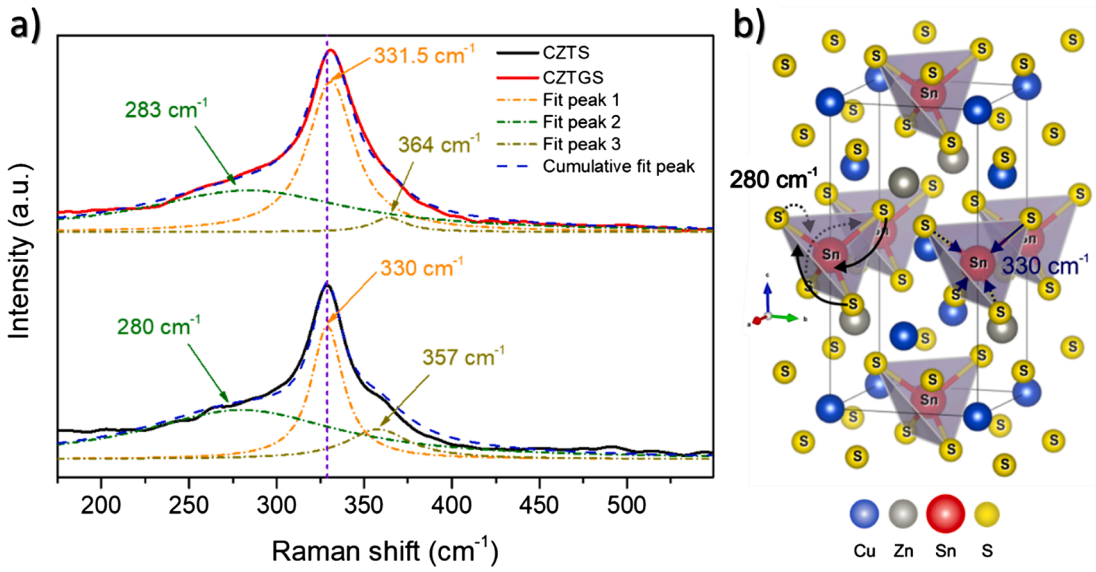

Fig. 4. (a) Room temperature Raman spectra of the CZTS and CZTGS nanoparticles and their Lorentzian deconvolutions, (b) schematic presentation of the rotation (around c-axis) and stretching vibration (around Sn) of Sn-S bonds in SnS_4 tetrahedra in Cu_2ZnSnS_4 lattice.

Cu_{Zn} antisite and V_{Cu} induces the p-type conductivity of Cu_2ZnSnS_4 kesterite. Meanwhile, the Zn_{Cu} antisite forms a shallow level near the conduction band that repels the holes and helps to collect the minority charge carrier in photovoltaic device [11]. However, the concentration of Cu_{Zn} and Zn_{Cu} antisite defects determines the degree of disorder in the kesterite structure [9–11]. The full width at half maximum (FHWM) of the principal A mode of CZTS (appeared around 330 cm^{-1} in our sample) has been associated to the existence of structural inhomogeneities within the disordered cation sublattice in the kesterite structure due to the formation of Cu_{Zn} and Zn_{Cu} antisites [51]. The FWHM of the A mode near 330 cm^{-1} (Fig. 4) increased due to incorporation of Ge in the CZTS nanostructures. The FWHM of the dispersion band for the CZTS and CZTGS nanostructures were 22 cm^{-1} and 41 cm^{-1}, respectively, indicating that the CZTGS nanostructures have higher structural disorder than in the CZTS nanostructures.

As the optical properties of CZTS and CZTGS nanoparticles are important parameters for their application as solar cell absorber material, we recorded their diffuse reflectance spectra in 300–1500 nm

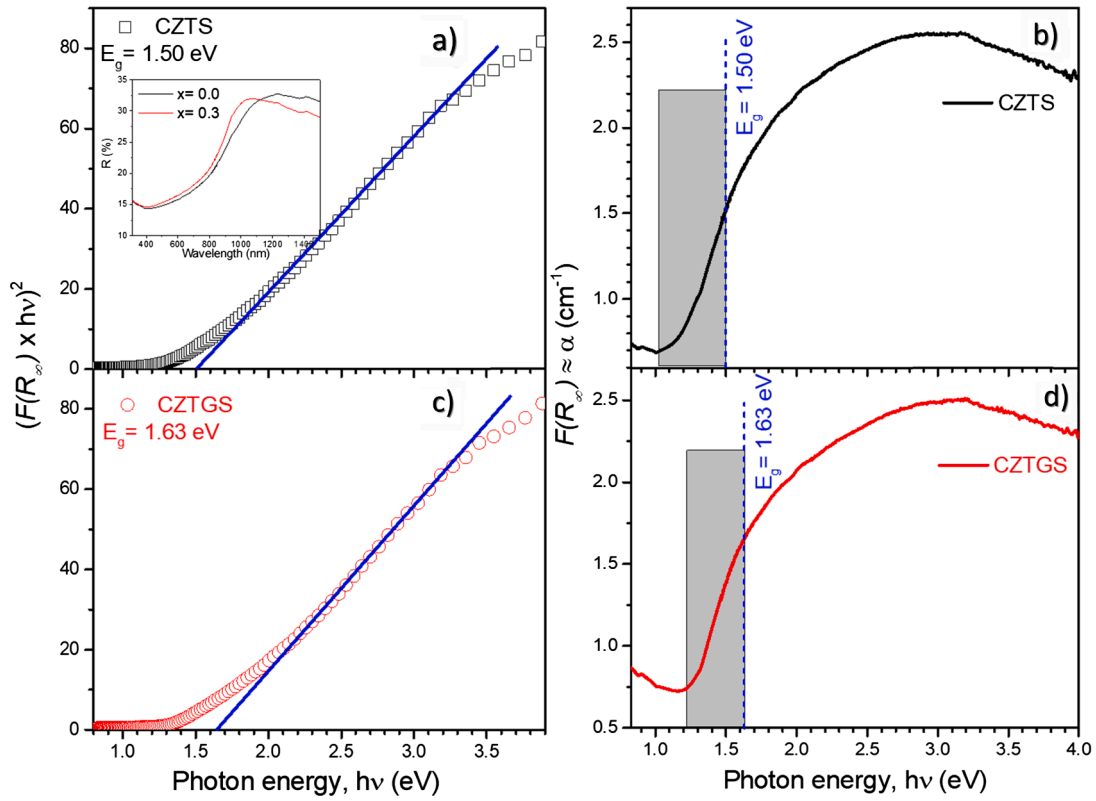

Fig. 5. The K-M plots used to estimate the optical band gap energies of (a) CZTS and (c) CZTGS nanoparticles. DRS spectra of the samples are presented in the inset of (a). K-M coefficient plots of the samples presented in (b, d) demonstrate their band tail regions (gray colored regions).

wavelength range (insert of Fig. 5a). The reflectance of both the samples decreased sharply at wavelengths below 950 nm, indicating their strong absorbance in the visible spectral range. The Kubelka Munk (K-M) formalism (Eq. (1)) was used to estimate the optical band gap of the nanoparticles [58,59]:

$$F(R_\infty) = \frac{(1-R_\infty)^2}{2R_\infty} = \frac{K}{S} \quad (1)$$

where K and S are the absorption and scattering coefficient of the sample, and R_∞ is the reflectance at infinite thickness of the sample. Fig. 5(a, c) shows the K-M plots for the samples with linear extrapolation to determine their band gap energy values. The optical band gap energy values for the CZTS and CZTGS nanostructures were estimated to be 1.50 and 1.63 eV, respectively, indicating an enhancement in band gap energy due to the substitution of Sn by Ge. The estimated band gap energy values of the samples are in good agreement with their values reported in the literature [19,20,22]. According to the literature, the kesterite Cu_2ZnSnS_4 presents band tail (absorption tail) owing to its structural disorder and high defect concentration [60,61]. Thus, the diffuse reflectance spectra of the samples were utilized to estimate their tentative Urbach energies using K-M formalism. The K-M absorption coefficient K becomes equal to 2α (α is the linear absorption coefficient of the material) when the material scatters in perfectly diffuse manner. Therefore, the K-M coefficient $F(R_\infty)$ is proportional to the absorbance of the material and its $F(R_\infty)$ plot is analogous to the absorbance spectrum. As can be seen in the $F(R_\infty)$ plots presented in Fig. 5(b,d), the band tail regions (gray zone) of both the samples remain close to their optical band gap edges. In band tail region, the spectral dependence of the absorption coefficient can be approximated with Urbach's empirical rule, which is given by the equation [62]:

$$\alpha = \alpha_0 e^{\left(\frac{h\nu}{E_u}\right)} \quad (2)$$

where α_0 is a constant and E_u is the energy of the band tail or Urbach energy. To estimate the Urbach energy values, we performed the $\ln(F(R_\infty))$ vs. photon energy plots for the samples (Fig. 6) and interpolated the linear regions (band tail region). Urbach energy values were estimated from the slopes of the linear fits.

Estimated Urbach energy values for the CZTS and CZTGS nanoparticles were 469 and 390 meV, respectively. It should be noted that the Urbach energy value we estimated for the CZTS nanostructures is considerably higher than its values reported (30–125 meV) in the literature [60,61,63]. The difference between the reported and estimated Urbach energy values for the samples probably lies in our approximation, where we considered the scattering coefficient S a constant, i.e., independent of excitation wavelength and there exists no boundary reflection (when the average grain size is larger than the wavelength) [58,59]. However, as we can see in Fig. 6, the Urbach energy value for the CZTS nanostructures decreased on substituting Sn by Ge. The principal origin of band tails in the kesterite Cu_2ZnSnS_4 is the $[2Cu_{Zn} + Sn_{Zn}]$ defect complex [60]. Therefore, the obtained results clearly indicate that substitution of Sn by Ge affects the formation of Sn_{Zn} antisite defects, causing a decrease of $[2Cu_{Zn} + Sn_{Zn}]$ defect concentration and reduction of Urbach energy.

The Sn_{Zn} antisite defects are formed in CZTS (the sample without germanium) as the Sn^{4+} ions can occupy the Zn sites due to the similar ionic radii of Sn^{4+} (0.55 Å) and Zn^{2+} (0.6 Å) ions. On the other hand, Ge^{4+} ions hardly occupy Zn sites, due to the smaller size of Ge^{4+} ions (0.39 Å) in comparison to the size of Zn^{2+} ions. Therefore, the concentrations of Sn_{Zn} and $(Cu_{Zn} + Sn_{Zn})$ defect complex are much lower in the sample containing germanium.

To understand the electrical conduction behavior of the fabricated kesterite nanostructures (CZTS and CZTGS), electrical resistivity (ρ), carrier concentration (p), and carrier mobility (μ) of the pelletized samples were measured in 100–320 K temperature interval. A typical pellet sample mounted over the ETO (electrical transport option) puck of the PPMS with electrical contacts is shown in Fig. 7a. A current was flown between the I_1^+ to I_1^- terminals and the voltage drop across V_1^+ and V_1^- terminals was measured to determinate the resistance of the sample. To calculate the resistivity of the sample, we use the four-probe method considering the sample geometry: [64]

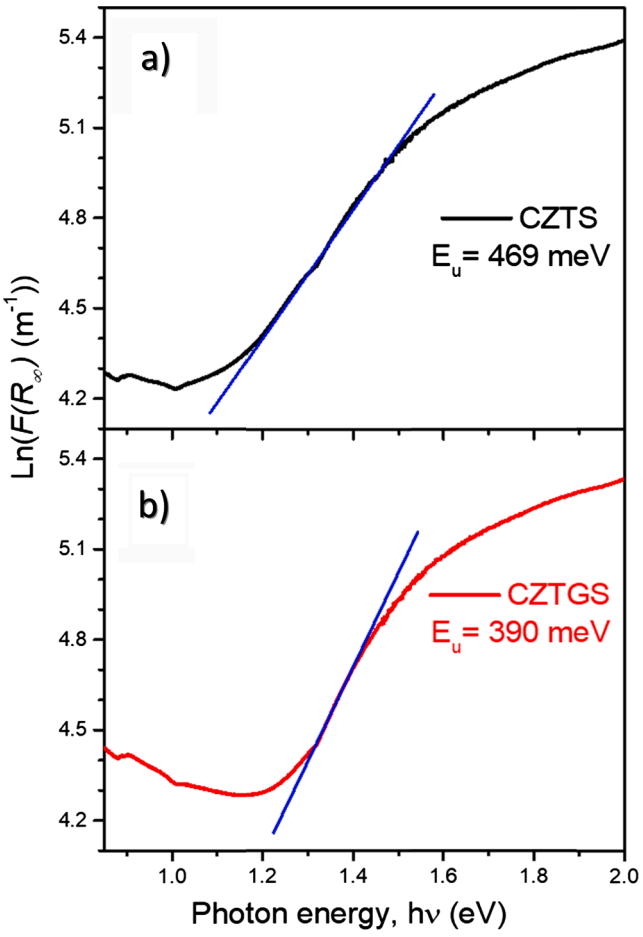

Fig. 6. Plots of $\ln(F(R_\infty))$ vs hν used to estimate the Urbach energy of (a) CZTS and (b) CZTGS nanoparticles.

$$\rho = \frac{\pi}{ln(2)} GR \quad (3)$$

where G is a correction factor ($G = (0.998\pi t)/\ln(2)$) equal to 3.483 and 3.664 mm for the CZTS and CZTGS sample, respectively; and R is the resistance of the sample. Fig. 7b shows the temperature variation of resistivity of the samples in 100–320 K range. As can be seen, the resistivity of CZTS decreased due to incorporation of Ge in the kesterite lattice. Room temperature (300 K) resistivity of the CZTS nanoparticles decreased from 415.48 Ωcm to 99.27 Ωcm on substituting 30% of Sn by Ge (Table 3). The estimated resistivities of the kesterite nanostructures are in good agreement with their values reported in the literature [3,20,35]. The Hall voltage was measured by flowing 0.1 mA current across the I_2^+ to I_2^- terminals and applying 5.0 T magnetic field perpendicular to the sample surface. Both the samples revealed positive Hall voltage, indicating their p-type conductivity. Hole concentrations in the samples were estimated using Eq. (4), where t is the thickness of the pellet (0.77 mm and 0.81 mm for CZTS and CZTGS samples, respectively).

$$p = \frac{BI}{V_H tq} \quad (4)$$

The variations of hole concentration in the samples with temperature

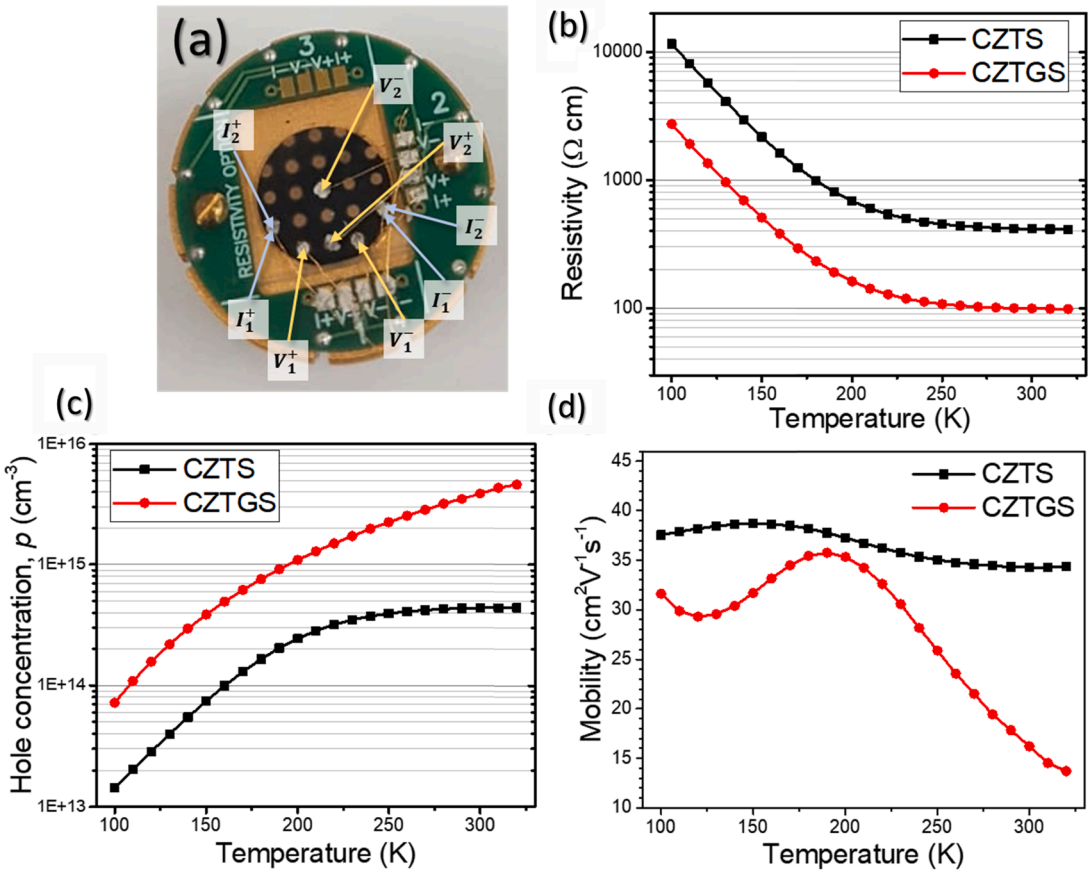

Fig. 7. (a) Photograph showing a typical sample mounting over PPMS puck with electrical contacts; and temperature variations of (b) resistivity, (c) hole concentration, (d) and carrier mobility in the CZTS and CZTGS nanostructures.

Table 3
Estimated electrical transport parameters of CZTS and CZTGS nanoparticles at 300 (room temperature) and 100 K.

Parameters	CZTS		CZTGS	
	100 K	300 K	100 K	300 K
resistivity (Ω cm)	11556.30	415.48	2732.66	99.27
hole concentration (cm^{-3})	1.43×10^{13}	4.38×10^{14}	7.22×10^{13}	3.88×10^{15}
hole mobility ($cm^2V^{-1}s^{-1}$)	37.54	34.25	31.62	16.21

are presented in Fig. 7c. As can be seen in this figure, the hole concentration at room temperature in CZTGS (~10^{15} cm^{-3}) is higher than CZTS by almost an order of magnitude (~10^{14} cm^{-3}). The room temperature hole concentrations (Table 3) estimated from Hall voltage are 4.38 × 10^{14} cm^{-3} and 3.87 × 10^{15} cm^{-3} for the CZTS and CZTGS nanostructures, respectively, which are in good agreement with their literature reported values [3,20,65]. From the estimated resistivity and hole concentration, we determined the carrier mobility (μ) in the samples using Eq. (5):

$$\mu = \frac{1}{\rho p q} \tag{5}$$

where ρ is the resistivity, p is the hole concentration, and q is the electronic charge. Temperature variations of hole mobility in the CZTS and CZTGS nanostructures are presented in Fig. 7d.

The observed increase in hole concentration and decrease in resistivity of CZTS nanostructures due to Ge incorporation are closely associated with the change in defect concentration in their electronic band gap [20]. As has been discussed earlier, the presence of Cu_{Zn} antisite and V_{Cu} defects in the kesterite lattice is responsible for its p-type conductivity. The EDS results presented in Table 1 indicate that on replacing 30% Sn atoms by Ge, while the Cu/(Zn + Sn + Ge) fraction remained fixed at 0.98, the Zn/(Sn + Ge) fraction in the CZTS lattice increased from 1.15 to 1.41. This clearly indicates an increase in Zn fraction in the kesterite lattice, which increases the concentration of (V_{Cu} + Zn_{Cu}) defect complex in the sample. As we can see in Fig. 7, at room temperature, the hole concentration in the CZTGS nanoparticles increased along with a reduction of charge carrier mobility. While the increase of carrier concentration in the sample is due to an increase of V_{Cu} concentration, the decrease of hole mobility is due to the increase of Zn_{Cu} concentration in the sample.

In fact, a substantial increase in the FWHM of the principal A mode (331.5 cm^{-1}) in the Raman spectrum of the CZTGS sample supports this assumption. On the other hand, due to incorporation of Ge, the concentration of Sn_{Zn} antisites decreased, as has been confirmed by the decrease in Urbach energy of the CZTGS sample. According to the previous reports, the Cu_{Zn} antisite and V_{Cu} defects form an acceptor level (at 63 to 132 meV over the valence band) and contribute to the p-type conductivity in Cu_2ZnSnS_4 kesterite [9,65–67]. We estimated the activation energy (E_a) of this acceptor level (associated with Cu_{Zn} and V_{Cu} defects) using the logarithm of the Arrhenius equation [67]:

$$\sigma(T) = \sigma_0 e^{-\left(\frac{E_a}{k_B T}\right)} \quad (6)$$

where $\sigma(T)$ is the conductivity of the sample at a particular temperature T, k_B is the, Boltzmann constant, σ_0 is the conductivity of the sample at absolute zero, and E_a is the activation energy. Fig. 8 shows the ln(σ) vs 1000/T plots for the CZTS and CZTGS nanoparticles in the 100–320 K temperature range. From the slopes of the linear interpolations of ln(σ), we estimated the activation energies of Cu_{Zn} antisites and V_{Cu} in CZTS and CZTGS nanostructures as 56.0 and 55.9 meV, respectively, which are close to their reported values [9,65–67]. While the results obtained from Raman analysis indicate an increase in concentration of Cu_{Zn} and Zn_{Cu} antisite defects in the CZTGS nanostructures, almost no change in position (or activation energy) of this acceptor level in the two samples (CZTS and CZTGS) clearly indicates the presence of these defects in both the sample, preserving their p-type electrical conductivity. Moreover, the increase in ($V_{Cu} + Zn_{Cu}$) antisite defect complex concentration in the CZTGS nanostructures increases their carrier (hole) concentration. As can be seen in Fig. 7c, incorporation of Ge in the kesterite lattice does not affect its usual semiconducting behavior throughout the measured temperature range.

Room temperature hole mobility in the CZTS nanostructures was estimated to be about 34.25 $cm^2V^{-1}S^{-1}$ (Table 3), which is considerably higher than the hole mobility values reported for CZTS nanoparticles (~25.4 $cm^2V^{-1}S^{-1}$) prepared by solvothermal process [20] and polycrystalline thin films (8.9–19.4 $cm^2V^{-1}S^{-1}$) prepared by physical and chemical deposition processes [3,4,68]. However, the hole mobility of the nanostructures decreased from 34.25 to 16.21 $cm^2V^{-1}S^{-1}$ (Table 3) on incorporating Ge (30% Sn substitution by Ge). As can be noticed in Fig. 7, the trend of variation of resistivity, hole concentration and mobility of charge carriers in the samples remain same even above the room temperature (up to 320 K).

In a semiconductor, the mobility and carrier concentration are temperature dependent. Moreover, the mobility of charge carriers in a semiconductor is controlled mainly by two processes: i) lattice scattering and ii) defect scattering [69]. As can be seen in Fig. 7d, the hole mobility of the CZTS nanostructures increased gradually with the decrease of temperature in the 320–150 K range, indicating a usual lattice scattering limited conduction in the semiconducting nanocrystals [69]. However, below 150 K, the hole mobility decreased slowly on decreasing the sample temperature, indicating a defect induced hopping conduction in this temperature range [70,71]. On the other hand, in the case of CZTGS nanocrystals, the hole mobility revealed a normal lattice scattering controlled transport behavior (i.e., increase of mobility with the decrease of temperature) above 200 K (200–320 K). However, at lower temperatures (<200 K), the mobility decreased gradually, indicating that defect scattering plays important role in this temperature region [70,71]. The temperatures of mobility maxima (150 K for CZTS and 200 K for CZTGS) can be considered as the onset temperatures, where the transition from lattice scattering controlled transport to hopping transport (through impurity scattering) occurs in the kesterite nanostructures. According to previous reports, the Cu_2ZnSnS_4 polycrystalline thin films [72,73], powder [66], and single crystals [65,71] present Mott variable-range hopping conduction in 30–230 K temperature range. In fact, the temperature of transition from lattice scattering controlled conduction to hopping conduction in CZTS has been seen to occur in the order: powder (100–230 K) > polycrystalline thin film (70–170 K) > single crystal (<100 K), which clearly indicates the contribution of defect structure on this parameter. Therefore, incorporation of Ge in the kesterite lattice apparently induces an early transition (from lattice scattering controlled conduction to hopping conduction), caused by the increment of Cu_{Zn} and Zn_{Cu} antisite defects concentration due to Ge incorporation.

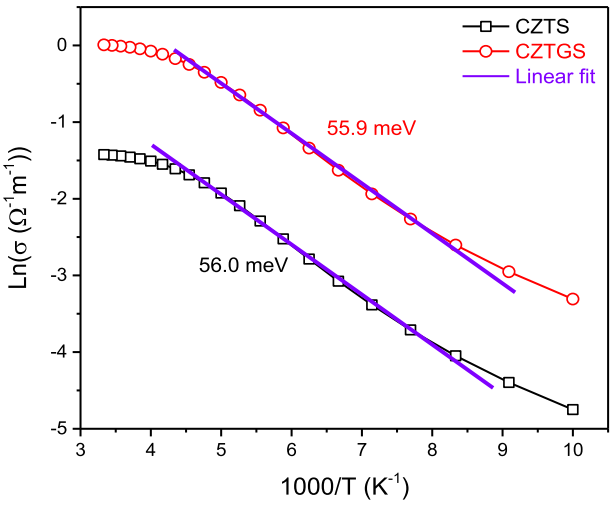

Fig. 8. Temperature dependence of the logarithm conductivity of CZTS and CZTGS nanoparticles to determine the activation energy.

The results presented in this article demonstrate that on incorporating a limited amount of Ge, it is possible to enhance the electrical conductivity of CZTS nanocrystal about four times, without sacrificing their carrier mobility considerably. Such a limited incorporation of Ge (x = 0.3) into CZTS lattice also avoids the formation of undesired phases (e.g., ZnS, Cu_xS, Cu_2SnS_3) which normally impose restrictions for the utilization of CZTGS nanostructures in photovoltaic devices [9,15,20]. Temperature dependent electrical transport behaviors of the kesterite nanostructures indicate that at room temperature, the hole transport in these p-type semiconductor nanocrystals is controlled by lattice scattering. Whereas, at low temperature the hole transport is controlled by defect scattering. The transition from predominant lattice scattering to predominant defect scattering controlled carrier transport occurs at a certain temperature, depending on the defect concentration in the kesterite nanostructures. While this transition occurs around 150 K in the CZTS nanocrystals, it shifts to about 200 K for CZTGS nanocrystals, probably due to the enhanced concentration of Cu_{Zn} and Zn_{Cu} antisites.

4. Conclusions

In summary, we could successfully synthesize phase pure, quasi-spherical $Cu_2ZnSn_{1-x}Ge_xS_4$ (x = 0.0 and 0.3) nanoparticles of 10–35 nm size range through a low-temperature hydrothermal process. The kesterite nanoparticles posse good crystallinity and free from any undesired secondary phase. Incorporation of Ge in the kesterite lattice induces the formation of ($V_{Cu} + Zn_{Cu}$) antisite complex and reduces the concentration of Sn_{Zn} antisite defects. Formation of Cu vacancies (V_{Cu}) in the kesterite lattice enhances hole concentration in the nanostructures, causing about one order increase of their electrical conductivity. However, the incorporation of Ge at Sn sites of the kesterite lattice does not affect the position of the acceptor level associated with Cu_{Zn} antisites and Cu vacancies (V_{Cu}) in their band structure. Temperature dependent electrical characterization revealed that depending on temperature, carrier transport in the kesterite nanocrystals is controlled either by lattice scattering or defect scattering. Cu_{Zn} and Zn_{Cu} antisite defects induce a transition from lattice scattering controlled conduction to hopping conduction. The results presented in this work indicate the CZTGS nanoparticles synthesized by substituting 30% Sn by Ge atoms in CZTS nanoparticles very attractive absorber layer material in photovoltaic devices.

CRediT authorship contribution statement

Umapada Pal: Conceptualization, Planning, Fund raising, Supervision, Writing and Reviewing. **Francisco Enrique Cancino-Gordillo:** Execution of experiments, Manuscript preparation. **Julio Villanueva Cab:** Writing and Reviewing.

Declaration of Competing Interest

The authors declare that they have no known competing financial interests or personal relationships that could have appeared to influence the work reported in this paper.

Acknowledgements

This work was supported by CONACyT (Grant # CB 2017-2018/A1-S-26720), Mexico. FECG acknowledges CONACyT, Mexico, for the doctoral fellowship (CVU # 784149).

References

[1] Y. Cao, M.S. Denny, J.V. Caspar, W.E. Farneth, Q. Guo, A.S. Ionkin, L.K. Johnson, M. Lu, I. Malajovich, D. Radu, H.D. Rosenfeld, K.R. Choudhury, W. Wu, High-Efficiency Solution-Processed $Cu_2ZnSn(S, Se)4$ Thin-Film Solar Cells Prepared from Binary and Ternary Nanoparticles, J. Am. Chem. Soc. 134 (2012) 15644–15647, https://doi.org/10.1021/ja3057985.

[2] S.-Y. Wei, Y.-C. Liao, C.-H. Hsu, C.-H. Cai, W.-C. Huang, M.-C. Huang, C.-H. Lai, Achieving high efficiency $Cu_2ZnSn(S, Se)4$ solar cells by non-toxic aqueous ink: Defect analysis and electrical modeling, Nano Energy 26 (2016) 74–82, https://doi.org/10.1016/j.nanoen.2016.04.059.

[3] D. Mora-Herrera, R. Silva-González, F.E. Cancino-Gordillo, M. Pal, Development of Cu_2ZnSnS_4 films from a non-toxic molecular precursor ink and theoretical investigation of device performance using experimental outcomes, Sol. Energy 199 (2020) 246–255, https://doi.org/10.1016/j.solener.2020.01.077.

[4] Y.-P. Lin, T.-E. Hsieh, Y.-C. Chen, K.-P. Huang, Characteristics of $Cu_2ZnSn(S_xSe_{1-x})_4$ thin-film solar cells prepared by sputtering deposition using single quaternary Cu_2ZnSnS_4 target followed by selenization/sulfurization treatment, Sol. Energy Mater. Sol. Cell. 162 (2017) 55–61, https://doi.org/10.1016/j.solmat.2016.12.042.

[5] I.G. Orletskyi, M.M. Solovan, V.V. Brus, F. Pinna, G. Cicero, P.D. Maryanchuk, E. V. Maistruk, M.I. Ilashchuk, T.I. Boichuk, E. Tresso, Structural, optical and electrical properties of Cu_2ZnSnS_4 films prepared from a non-toxic DMSO-based sol-gel and synthesized in low vacuum, J. Phys. Chem. Solids 100 (2017) 154–160, https://doi.org/10.1016/j.jpcs.2016.09.015.

[6] C. Yan, J. Huang, K. Sun, S. Johnston, Y. Zhang, H. Sun, A. Pu, M. He, F. Liu, K. Eder, L. Yang, J.M. Cairney, N.J. Ekins-Daukes, Z. Hameiri, J.A. Stride, S. Chen, M.A. Green, X. Hao, Cu_2ZnSnS_4 solar cells with over 10% power conversion efficiency enabled by heterojunction heat treatment, Nat. Energy. 3 (2018) 764–772, https://doi.org/10.1038/s41560-018-0206-0.

[7] W. Wang, M.T. Winkler, O. Gunawan, T. Gokmen, T.K. Todorov, Y. Zhu, D.B. Mitzi, Device Characteristics of CZTSSe Thin-Film Solar Cells with 12.6% Efficiency, Adv. Energy Mater. 4 (2014) 1301465, https://doi.org/10.1002/aenm.201301465.

[8] K. Pal, P. Singh, A. Bhaduri, K.B. Thapa, Current challenges and future prospects for a highly efficient (20%) kesterite CZTS solar cell: A review, Sol. Energy Mater. Sol. Cell. 196 (2019) 138–156, https://doi.org/10.1016/j.solmat.2019.03.001.

[9] S. Schorr, G. Gurieva, M. Guc, M. Dimitrievska, A. Pérez-Rodríguez, V. Izquierdo-Roca, C.S. Schnohr, J. Kim, W. Jo, J.M. Merino, Point defects, compositional fluctuations, and secondary phases in non-stoichiometric kesterites, J. Phys. Energy 2 (2019) 012002, https://doi.org/10.1088/2515-7655/ab4a25.

[10] M. Grossberg, J. Krustok, C.J. Hages, D.M. Bishop, O. Gunawan, R. Scheer, S. M. Lyam, H. Hempel, S. Levcenco, T. Unold, The electrical and optical properties of kesterites, J. Phys. Energy 1 (2019) 044002, https://doi.org/10.1088/2515-7655/ab29a0.

[11] M. Kumar, A. Dubey, N. Adhikari, S. Venkatesan, Q. Qiao, Strategic review of secondary phases, defects and defect-complexes in kesterite CZTS–Se solar cells, Energy Environ. Sci. 8 (2015) 3134–3159, https://doi.org/10.1039/C5EE02153G.

[12] K. Biswas, S. Lany, A. Zunger, The electronic consequences of multivalent elements in inorganic solar absorbers: Multivalency of Sn in Cu_2ZnSnS_4, Appl. Phys. Lett. 96 (2010) 201902, https://doi.org/10.1063/1.3427433.

[13] X. Lv, C. Zhu, H. Hao, R. Liu, Y. Wang, J. Wang, Improving the performance of low-cost water-based solution-synthesised $Cu_2ZnSn_{1-x}Ge_x(S, Se)4$ absorber thin films by germanium doping, Ceram. Int. 46 (2020) 25638–25645, https://doi.org/10.1016/j.ceramint.2020.07.039.

[14] S. Kim, K.M. Kim, H. Tampo, H. Shibata, K. Matsubara, S. Niki, Ge-incorporated $Cu_2ZnSnSe_4$ thin-film solar cells with efficiency greater than 10%, Sol. Energy Mater. Sol. Cell. 144 (2016) 488–492, https://doi.org/10.1016/j.solmat.2015.09.039.

[15] M. Neuschitzer, M.E. Rodriguez, M. Guc, J.A. Marquez, S. Giraldo, I. Forbes, A. Perez-Rodriguez, E. Saucedo, Revealing the beneficial effects of Ge doping on $Cu_2ZnSnSe_4$ thin film solar cells, J. Mater. Chem. A 6 (2018) 11759–11772, https://doi.org/10.1039/C8TA02551G.

[16] C.J. Hages, S. Levcenco, C.K. Miskin, J.H. Alsmeier, D. Abou-Ras, R.G. Wilks, M. Bär, T. Unold, R. Agrawal, Improved performance of Ge-alloyed CZTGeSSe thin-film solar cells through control of elemental losses, Prog. Photovoltaics Res. Appl. 23 (2015) 376–384, https://doi.org/10.1002/pip.2442.

[17] S. Giraldo, M. Neuschitzer, T. Thersleff, S. López-Marino, Y. Sánchez, H. Xie, M. Colina, M. Placidi, P. Pistor, V. Izquierdo-Roca, K. Leifer, A. Pérez-Rodríguez, E. Saucedo, Large Efficiency Improvement in $Cu_2ZnSnSe_4$ Solar Cells by Introducing a Superficial Ge Nanolayer, Adv. Energy Mater. 5 (2015) 1501070, https://doi.org/10.1002/aenm.201501070.

[18] S. Kim, K.M. Kim, H. Tampo, H. Shibata, S. Niki, Improvement of voltage deficit of Ge-incorporated kesterite solar cell with 12.3% conversion efficiency, Appl. Phys. Express 9 (2016) 102301, https://doi.org/10.7567/APEX.9.102301.

[19] Y. Li, W. Ling, Q. Han, W. Shi, Colloidal $Cu_2Zn(Sn_{1-x}Ge_x)S_4$ nanocrystals: electrical properties and comparison between their wurtzite and kesterite structures, RSC Adv. 4 (2014) 55016–55022, https://doi.org/10.1039/C4RA10780B.

[20] D. Mora-Herrera, M. Pal, F. Paraguay-Delgado, Facile solvothermal synthesis of $Cu_2ZnSn_{1-x}Ge_xS_4$ nanocrystals: Effect of Ge content on optical and electrical properties, Mater. Chem. Phys. 257 (2021) 123764, https://doi.org/10.1016/j.matchemphys.2020.123764.

[21] E. Garcia-Llamas, J.M. Merino, R. Serna, X. Fontané, I.A. Victorov, A. Pérez-Rodríguez, M. León, I.V. Bodnar, V. Izquierdo-Roca, R. Caballero, Wide band-gap tuning $Cu_2ZnSn_{1-x}Ge_xS_4$ single crystals: Optical and vibrational properties, Sol. Energy Mater. Sol. Cell. 158 (2016) 147–153, https://doi.org/10.1016/j.solmat.2015.12.021.

[22] X. Peng, S. Zhang, Y. Xiang, Solvothermal synthesis of $Cu_2Zn(Sn_{1-x}Ge_x)S_4$ and $Cu_2(Sn_{1-x}Ge_x)S_3$ nanoparticles with tunable band gap energies, J. Alloys Compd. 640 (2015) 75–81, https://doi.org/10.1016/j.jallcom.2015.03.248.

[23] D.B. Khadka, J.H. Kim, Band gap engineering of alloyed $Cu_2ZnGe_xSn_{1-x}Q_4$ (Q = S, Se) films for solar cell, J. Phys. Chem. C 119 (2015) 1706–1713, https://doi.org/10.1021/jp510877g.

[24] M. Neuschitzer, J. Marquez, S. Giraldo, M. Dimitrievska, M. Placidi, I. Forbes, V. Izquierdo-Roca, A. Pérez-Rodriguez, E. Saucedo, V_{oc} Boosting and Grain Growth Enhancing Ge-Doping Strategy for $Cu_2ZnSnSe_4$ Photovoltaic Absorbers, J. Phys. Chem. C 120 (2016) 9661–9670, https://doi.org/10.1021/acs.jpcc.6b02315.

[25] W. Xie, X. Jiang, C. Zou, D. Li, J. Zhang, J. Quan, L. Shao, Synthesis of highly dispersed Cu_2ZnSnS_4 nanoparticles by solvothermal method for photovoltaic application, Physica E 45 (2012) 16–20, https://doi.org/10.1016/j.physe.2012.05.022.

[26] W.-H. Zhou, Y.-L. Zhou, J. Feng, J.-W. Zhang, S.-X. Wu, X.-C. Guo, X. Cao, Solvothermal synthesis of flower-like Cu_2ZnSnS_4 nanostructures and their application as anode materials for lithium-ion batteries, Chem. Phys. Lett. 546 (2012) 115–119, https://doi.org/10.1016/j.cplett.2012.07.060.

[27] M. Zhou, Y. Gong, J. Xu, G. Fang, Q. Xu, J. Dong, Colloidal CZTS nanoparticles and films: Preparation and characterization, J. Alloys Compd. 574 (2013) 272–277, https://doi.org/10.1016/j.jallcom.2013.05.143.

[28] A.G. Kannan, T.E. Manjulavalli, J. Chandrasekaran, Influence of Solvent on the Properties of CZTS Nanoparticles, Procedia Eng. 141 (2016) 15–22, https://doi.org/10.1016/j.proeng.2015.08.1112.

[29] A. Méndez-López, A. Morales-Acevedo, Y.J. Acosta-Silva, M. Ortega-López, Synthesis and Characterization of Colloidal CZTS Nanocrystals by a Hot-Injection Method, J. Nanomaterials 2016 (2016) 1–7, https://doi.org/10.1155/2016/7486094.

[30] J. Li, X. Gao, L. Han, X. Yang, H. Liu, L-cystine-assisted synthesis of Cu_2ZnGeS_4 nanocrystal powder via solvothermal process, Mater. Lett. 163 (2016) 111–114, https://doi.org/10.1016/j.matlet.2015.10.065.

[31] R. Caballero, J.M. Cano-Torres, E. Garcia-Llamas, X. Fontané, A. Pérez-Rodríguez, D. Greiner, C.A. Kaufmann, J.M. Merino, I. Victorov, G. Baraldi, M. Valakh, I. Bodnar, V. Izquierdo-Roca, M. León, Towards the growth of $Cu_2ZnSn_{1-x}Ge_xS_4$ thin films by a single-stage process: Effect of substrate temperature and composition, Sol. Energy Mater. Sol. Cell. 139 (2015) 1–9, https://doi.org/10.1016/j.solmat.2015.03.004.

[32] J.R. González-Castillo, F.A. Pulgarín-Agudelo, E. Rodríguez-González, O. Vigil-Galán, M. Courel-Piedrahita, J.A. Andrade-Arvizu, Influence of Ge content on $Cu_2Zn(SnGe)Se_4$ physical properties deposited by sequential thermal evaporation technique, Mater. Sci. Semicond. Process. 83 (2018) 96–101, https://doi.org/10.1016/j.mssp.2018.04.024.

[33] M. Courel, T.G. Sanchez, N.R. Mathews, X. Mathew, Cu_2ZnGeS_4 thin films deposited by thermal evaporation: the impact of Ge concentration on physical properties, J. Phys. D 51 (2018) 095107, https://doi.org/10.1088/1361-6463/aaa7db.

[34] M. Grossberg, K. Timmo, T. Raadik, E. Kärber, V. Mikli, J. Krustok, Study of structural and optoelectronic properties of $Cu_2Zn(Sn_{1-x}Ge_x)Se_4$ (x= 0 to 1) alloy compounds, Thin Solid Films 582 (2015) 176–179, https://doi.org/10.1016/J.TSF.2014.10.055.

[35] M. Singh, T.R. Rana, J.H. Kim, Fabrication of band gap tuned $Cu_2Zn(Sn_{1-x}Ge_x)(S, Se)_4$ absorber thin film using nanocrystal-based ink in non-toxic solvent, J. Alloys Compd. 675 (2016) 370–376, https://doi.org/10.1016/j.jallcom.2016.03.138.

[36] R.D. Shannon, Revised effective ionic radii and systematic studies of interatomic distances in halides and chalcogenides, Acta Crystallogr. Sect. A. 32 (1976) 751–767, https://doi.org/10.1107/S0567739476001551.

[37] B.H. Toby, R.B. Von Dreele, GSAS-II : the genesis of a modern open-source all purpose crystallography software package, J. Appl. Crystallogr. 46 (2013) 544–549, https://doi.org/10.1107/S0021889813003531.

[38] B.H. Toby, R factors in Rietveld analysis: How good is good enough? Powder Diffr. 21 (2006) 67–70, https://doi.org/10.1154/1.2179804.

[39] S. Schorr, The crystal structure of kesterite type compounds: A neutron and X-ray diffraction study, Sol. Energy Mater. Sol. Cell. 95 (2011) 1482–1488, https://doi.org/10.1016/j.solmat.2011.01.002.

[40] C.-M. Fan, M.D. Regulacio, C. Ye, S.H. Lim, S.K. Lua, Q.-H. Xu, Z. Dong, A.-W. Xu, M.-Y. Han, Colloidal nanocrystals of orthorhombic Cu_2ZnGeS_4: phase-controlled synthesis, formation mechanism and photocatalytic behavior, Nanoscale. 7 (2015) 3247–3253, https://doi.org/10.1039/C4NR07012G.

[41] C. Qin, L. Gao, E. Wang, Germanium: Inorganic Chemistry, in: Encycl. Inorg. Chem., John Wiley & Sons, Ltd, Chichester, UK, 2006, https://doi.org/10.1002/0470862106.ia079.

[42] M. Dimitrievska, F. Boero, A.P. Litvinchuk, S. Delsante, G. Borzone, A. Perez-Rodriguez, V. Izquierdo-Roca, Structural Polymorphism in "Kesterite" Cu_2ZnSnS_4: Raman Spectroscopy and First-Principles Calculations Analysis, Inorg. Chem. 56 (2017) 3467–3474, https://doi.org/10.1021/acs.inorgchem.6b03008.

[43] N. Kattan, B. Hou, D.J. Fermín, D. Cherns, Crystal structure and defects visualization of Cu_2ZnSnS_4 nanoparticles employing transmission electron microscopy and electron diffraction, Appl. Mater. Today 1 (2015) 52–59, https://doi.org/10.1016/j.apmt.2015.08.004.

[44] W.-S. Liu, S.-Y. Chen, C.-S. Huang, M.-Y. Lee, H.-C. Kuo, Investigation of Zn/Sn ratio for improving the material quality of CZTS thin films with the reduction of $Cu_{2-x}S$ secondary phase, J. Alloys Compd. 853 (2021) 157237, https://doi.org/10.1016/j.jallcom.2020.157237.

[45] X. Li, H. Cao, Y. Dong, F. Yue, Y. Chen, P. Xiang, L. Sun, P. Yang, J. Chu, Investigation of Cu_2ZnSnS_4 thin films with controllable Cu composition and its influence on photovoltaic properties for solar cells, J. Alloys Compd. 694 (2017) 833–840, https://doi.org/10.1016/j.jallcom.2016.10.024.

[46] J. Just, C.M. Sutter-Fella, D. Lützenkirchen-Hecht, R. Frahm, S. Schorr, T. Unold, Secondary phases and their influence on the composition of the kesterite phase in CZTS and CZTSe thin films, Phys. Chem. Chem. Phys. 18 (2016) 15988–15994, https://doi.org/10.1039/C6CP00178E.

[47] M. Dimitrievska, A. Fairbrother, E. Saucedo, A. Pérez-Rodríguez, V. Izquierdo-Roca, Influence of compositionally induced defects on the vibrational properties of device grade $Cu_2ZnSnSe_4$ absorbers for kesterite based solar cells, Appl. Phys. Lett. 106 (2015) 073903, https://doi.org/10.1063/1.4913262.

[48] M. Guc, S. Levcenko, I.V. Bodnar, V. Izquierdo-Roca, X. Fontane, L.V. Volkova, E. Arushanov, A. Pérez-Rodríguez, Polarized Raman scattering study of kesterite type Cu_2ZnSnS_4 single crystals, Sci. Rep. 6 (2016) 19414, https://doi.org/10.1038/srep19414.

[49] M. Dimitrievska, A. Fairbrother, X. Fontané, T. Jawhari, V. Izquierdo-Roca, E. Saucedo, A. Pérez-Rodríguez, Multiwavelength excitation Raman scattering study of polycrystalline kesterite Cu_2ZnSnS_4 thin films, Appl. Phys. Lett. 104 (2014), https://doi.org/10.1063/1.4861593.

[50] D. Dumcenco, Y.-S.-S. Huang, The vibrational properties study of kesterite Cu_2ZnSnS_4 single crystals by using polarization dependent Raman spectroscopy, Opt. Mater. 35 (2013) 419–425, https://doi.org/10.1016/j.optmat.2012.09.031.

[51] M.Y. Valakh, O.F. Kolomys, S.S. Ponomaryov, V.O. Yukhymchuk, I.S. Babichuk, V. Izquierdo-Roca, E. Saucedo, A. Perez-Rodriguez, J.R. Morante, S. Schorr, I. V. Bodnar, Raman scattering and disorder effect in Cu_2ZnSnS_4, Phys. Stat. Sol. - Rapid Res. Lett. 7 (2013) 258–261, https://doi.org/10.1002/pssr.201307073.

[52] E. Garcia-Llamas, M. Guc, I.V. Bodnar, X. Fontané, R. Caballero, J.M. Merino, M. León, V. Izquierdo-Roca, Multiwavelength excitation Raman scattering of $Cu_2ZnSn_{1-x}Gex(S, Se)4$ single crystals for earth abundant photovoltaic applications, J. Alloys Compd. 692 (2017) 249–256, https://doi.org/10.1016/j.jallcom.2016.09.035.

[53] J.M. Cano-Torres, R. Caballero, I. Victorov, M. León, E. Garcia-Llamas, V. O. Yukhymchuk, A.M. Yaremko, Y.O. Havryliuk, I. Bodnar, J.M. Merino, Raman characterization and modelling of $Cu_2ZnSn_{1-x}Ge_xS_4$ single crystals grown using chemical vapor transport, Opt. Mater. 66 (2017) 671–677, https://doi.org/10.1016/j.optmat.2017.03.016.

[54] S. Chen, L.-W. Wang, A. Walsh, X.G. Gong, S.-H. Wei, Abundance of $Cu_{Zn} + Sn_{Zn}$ and $2Cu_{Zn} + Sn_{Zn}$ defect clusters in kesterite solar cells, Appl. Phys. Lett. 101 (2012) 223901, https://doi.org/10.1063/1.4768215.

[55] D. Han, Y.Y. Sun, J. Bang, Y.Y. Zhang, H.B. Sun, X. Bin Li, S.B. Zhang, Deep electron traps and origin of p-type conductivity in the earth-abundant solar-cell material Cu_2ZnSnS_4, Phys. Rev. B - Condens. Matter Mater. Phys. 87 (2013), https://doi.org/10.1103/PhysRevB.87.155206.

[56] S. Chen, A. Walsh, X.-G. Gong, S.-H. Wei, Classification of Lattice Defects in the Kesterite Cu_2ZnSnS_4 and $Cu_2ZnSnSe_4$ Earth-Abundant Solar Cell Absorbers, Adv. Mater. 25 (2013) 1522–1539, https://doi.org/10.1002/adma.201203146.

[57] H. Nishihara, T. Maeda, A. Shigemi, T. Wada, First-principles study of defect formation in the photovoltaic semiconductors Cu_2GeS_3 and Cu_2ZnGeS_4 for comparison with Cu_2SnS_3, Cu_2ZnSnS_4, and $CuInSe_2$, Jpn. J. Appl. Phys. 56 (2017) 04CS08, https://doi.org/10.7567/JJAP.56.04CS08.

[58] A. Escobedo Morales, E. Sánchez Mora, U. Pal, Use of diffuse reflectance spectroscopy for optical characterization of un-supported nanostructures, Rev. Mex. Fís. S 53 (2007) 18–22.

[59] R. Molenaar, J.J. ten Bosch, J.R. Zijp, Determination of Kubelka-Munk scattering and absorption coefficients by diffuse illumination, Appl. Opt. 38 (1999) 2068, https://doi.org/10.1364/AO.38.002068.

[60] G. Rey, G. Larramona, S. Bourdais, C. Choné, B. Delatouche, A. Jacob, G. Dennler, S. Siebentritt, On the origin of band-tails in kesterite, Sol. Energy Mater. Sol. Cell. 179 (2018) 142–151, https://doi.org/10.1016/j.solmat.2017.11.005.

[61] J.K. Larsen, J.J.S. Scragg, N. Ross, C. Platzer-Björkman, Band Tails and Cu–Zn Disorder in Cu_2ZnSnS_4 Solar Cells, ACS Appl. Energy Mater. 3 (2020) 7520–7526, https://doi.org/10.1021/acsaem.0c00926.

[62] I. Studenyak, M. Kranjec, M. Kurik, Urbach Rule in Solid State Physics, Int. J. Opt. Appl. 4 (2014) 76–83, https://doi.org/10.5923/j.optics.20140403.02.

[63] M. Valentini, C. Malerba, F. Menchini, D. Tedeschi, A. Polimeni, M. Capizzi, A. Mittiga, Effect of the order-disorder transition on the optical properties of Cu_2ZnSnS_4, Appl. Phys. Lett. 108 (2016) 211909, https://doi.org/10.1063/1.4952973.

[64] I. Miccoli, F. Edler, H. Pfnür, C. Tegenkamp, The 100th anniversary of the four-point probe technique: the role of probe geometries in isotropic and anisotropic systems, J. Phys.: Condens. Matter 27 (2015) 223201, https://doi.org/10.1088/0953-8984/27/22/223201.

[65] A. Nagaoka, H. Miyake, T. Taniyama, K. Kakimoto, K. Yoshino, Correlation between intrinsic defects and electrical properties in the high-quality Cu_2ZnSnS_4 single crystal, Appl. Phys. Lett. 103 (2013) 112107, https://doi.org/10.1063/1.4821279.

[66] E. Hajdeu-Chicarosh, M. Guc, K. Neldner, G. Gurieva, S. Schorr, E. Arushanov, K. G. Lisunov, Mechanisms of conductivity and energy spectrum of near-edge holes in Cu_2ZnSnS_4 powder samples, J. Alloys Compd. 703 (2017) 315–320, https://doi.org/10.1016/j.jallcom.2017.01.352.

[67] N. Muhunthan, O.P. Singh, V.N. Singh, K.N. Sood, Rashmi, Electric field-effect-assisted persistent photoconductivity in CZTS, Adv. Mater. Lett. 6 (2015) 290–293, https://doi.org/10.5185/amlett.2015.5704.

[68] X. Wu, W. Liu, S. Cheng, Y. Lai, H. Jia, Photoelectric properties of Cu_2ZnSnS_4 thin films deposited by thermal evaporation, J. Semicond. 33 (2012) 022002, https://doi.org/10.1088/1674-4926/33/2/022002.

[69] S. Kasap, C. Koughia, H.E. Ruda, Electrical Conduction in Metals and Semiconductors, in: S. Kasap, P. Capper (Eds.), Springer Handbook of Electronic and Photonic Materials. Springer Handbooks, Springer, Cham, 2017, https://doi.org/10.1007/978-3-319-48933-9_2.

[70] S. Schuler, S. Siebentritt, S. Nishiwaki, N. Rega, J. Beckmann, S. Brehme, M.C. Lux-Steiner, Self-compensation of intrinsic defects in the ternary semiconductor $CuGaSe_2$, Phys. Rev. B 69 (2004) 045210, https://doi.org/10.1103/PhysRevB.69.045210.

[71] A. Nagaoka, H. Miyake, T. Taniyama, K. Kakimoto, Y. Nose, M.A. Scarpulla, K. Yoshino, Effects of sodium on electrical properties in Cu_2ZnSnS_4 single crystal, Appl. Phys. Lett. 104 (2014) 152101, https://doi.org/10.1063/1.4871208.

[72] V. Kosyak, M.A. Karmarkar, M.A. Scarpulla, Temperature dependent conductivity of polycrystalline Cu_2ZnSnS_4 thin films, Appl. Phys. Lett. 100 (2012) 263903, https://doi.org/10.1063/1.4731875.

[73] M. Zubair Ansari, N. Khare, Thermally activated band conduction and variable range hopping conduction in Cu_2ZnSnS_4 thin films, J. Appl. Phys. 117 (2015) 025706, https://doi.org/10.1063/1.4905673.